Near-Field Ground Motion of the 2002 Denali Fault, Alaska, Earthquake Recorded at Pump Station 10

W. L. Ellsworth,[a] M. Celebi,[a] M.EERI, J. R. Evans,[a] E. G. Jensen,[a] R. Kayen,[a] M. C. Metz,[b] D. J. Nyman,[c] M.EERI, J. W. Roddick,[d] P. Spudich,[a] M.EERI, and C. D. Stephens[a]

A free-field recording of the Denali fault earthquake was obtained by the Alyeska Pipeline Service Company 3 km from the surface rupture of the Denali fault. The instrument, part of the monitoring and control system for the trans-Alaska pipeline, was located at Pump Station 10, approximately 85 km east of the epicenter. After correction for the measured instrument response, we recover a seismogram that includes a permanent displacement of 3.0 m. The recorded ground motion has relatively low peak acceleration (0.36 g) and very high peak velocity (180 cm/s). Nonlinear soil response may have reduced the peak acceleration to this 0.36 g value. Accelerations in excess of 0.1 g lasted for 10 s, with the most intense motion occurring during a 1.5-s interval when the rupture passed the site. The low acceleration and high velocity observed near the fault in this earthquake agree with observations from other recent large-magnitude earthquakes. [DOI: 10.1193/1.1778172]

INTRODUCTION

The M7.9* earthquake of 3 November 2002 ruptured 340 km of the Denali and related faults in the largest strike-slip earthquake in North America in almost 150 years (Eberhart-Phillips et al. 2003). The earthquake occurred beneath the spine of the Alaska Range, a rugged and remote mountain belt in central Alaska (Figure 1). The main shock initiated as a bilateral rupture on the 40-km-long Susitna Glacier fault before beginning its long, west-to-east strike-slip rupture on the Denali and Totschunda faults (Figure 1). The principal seismic energy release occurred on the 218-km-long ruptured segment of the Denali fault, where the right-lateral fault displacement averaged 5.0-5.3 m.

The nature of ground motion in large-magnitude earthquakes near the causative faults continues to be of critical interest to engineers and earth scientists alike because there are few observations with which to constrain either empirical or theoretical models (Somerville 2003, Campbell and Bozorgnia 2003, Lee et al. 2001). We are fortunate that such a record was obtained by the Alyeska Pipeline Service Company (hereinafter, Aly-

[a] U.S. Geological Survey, 345 Middlefield Road, Menlo Park, CA 94025
[b] M. C. Metz & Associates, 1049 W 5th Avenue, Anchorage, AK 99501
[c] D. J. Nyman & Associates, 12337 Jones Rd # 232, Houston, TX 77070
[d] Alyeska Pipeline Service Company, P.O. Box 60469, Fairbanks, AK 99706

* All magnitudes in this issue, unless otherwise indicated, are moment magnitudes, M.

Earthquake Spectra, Volume 20, No. 3, pages 597–615, August 2004; © 2004, Earthquake Engineering Research Institute

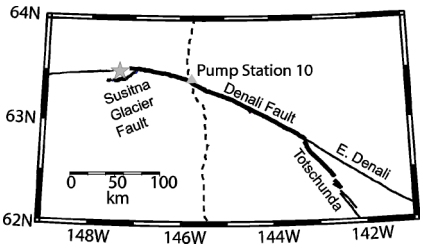

Figure 1. Location of the Denali Fault earthquake rupture (bold line) through the Alaska Range. Epicenter (star) of initial thrust rupture of the Susitna Glacier fault is located at the western end of this 340-km-long unilateral rupture. PS10 of the Alyeska Pipeline Service Company (triangle) is located 3 km ENE of the nearest point on the Denali fault. The pipeline route generally parallels the Richardson Highway (dashed).

eska) 3 km from where the Denali fault slipped 5-6 m horizontally and 0.5 m vertically in the earthquake. The combination of the close proximity to the fault and the large magnitude of the event make this an extremely rare and potentially important recording.

In this paper, we describe the calibration of the instrumentation and recording system, and the recovery of long-period (greater than 10 s) ground motions, compare the motion with building code response spectra, and discuss the ground motion implications for the faulting process. This paper supersedes the earlier report of Ellsworth et al. (2004) in which theoretical values were used for the recording system response instead of the measured values reported here.

INSTRUMENTATION AT PUMP STATION 10

A free-field strong-motion recording of the earthquake was obtained by Alyeska at Pump Station 10 (instrument station PS10) some 85 km east of the epicenter (Figure 1). Pump Station 10 had been "mothballed" six years before the earthquake, and piping, vessels and storage tanks were empty when the earthquake struck. The facility did not sustain any structural damage in the earthquake (Hall et al. 2003).

The instrument at PS10 is part of the accelerograph network operated by Alyeska to provide seismic alarms and response data for pipeline operations control. The instrument enclosure sits on Holocene gravels on level ground, approximately 50 m from the nearest buildings and pipeline infrastructure, on the eastern side of the 1.5-km-wide valley incised across the Alaska Range by the Delta River (Figure 2). The accelerometers are mounted on a grade-level concrete slab measuring 5 ft×5 ft×2 ft (1.52 m×1.52 m ×0.61 m). Boreholes to a depth of 30 m (National Soil Service 1971) show the deposits to be coarse-grained, mostly sand to silty gravel and gravelly sand up to boulder size, with an average blow count of about 50. The average shear-wave velocity in the upper 30 m is 316 m/s, and the shear-wave velocity exceeds 600 m/s at a depth of about 115 m (Kayen et al. 2004). Thus the site would be classified in *IBC2003* (International Code Council 2002) as site class D or soil type 3 in the 1994 *Uniform Building Code* (*UBC94*), (International Conference of Building Officials 1994), (or soil profile type S_D

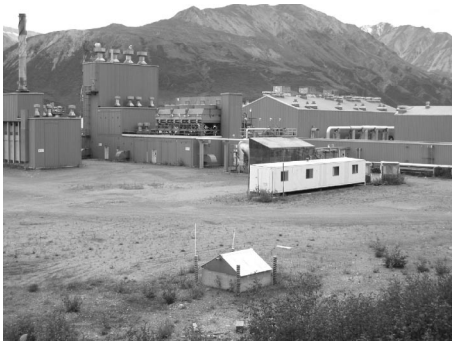

Figure 2. View of Alyeska Pipeline Service Company Pump Station 10 looking to northwest. Nearest point on the Denali fault is 3 km to the left (south). Strong-motion sensors are located in the small enclosure in the foreground. The Delta River lies between the pump station and the mountain in the distance.

in *UBC97*), and it would have a Geomatrix code of IHC (Electric Power Research Institute 1993).

The sensors are navigation-grade, Honeywell Sundstrand Q-Flex™ force-balance accelerometers, which are constructed by laser etching both the mass and a simple cantilever from a single piece of quartz and equipping this mechanical system with capacitive displacement sensing and electromagnetic force feedback. This is a robust sensor (250-g shock tolerance) with high natural frequency (higher than 800 Hz), small displacements, and excellent low cross-axis sensitivity (about 0.3%). The current in the force-feedback loop is the output signal, converted to a voltage in this application by passing it through a 1.91-KΩ resistor, and conditioned through a Honeywell Sundstrand amplifier. Compensation for individual sensor sensitivity factors is performed in software subsequent to band-pass filtering and 16-bit digitization. The signals are band-pass filtered between 0.086 Hz and 40 Hz by a pair of cascaded 2-pole analog Butterworth filters in the control room. The analog signals are digitized at 200 samples/s by a PC-based recording system in the control room. The dynamic range of the system is about ± 1.6 g.

INSTRUMENT CALIBRATION

In September 2003, Alyeska and the U.S. Geological Survey (USGS) embarked on a joint effort to test and calibrate the accelerometers, amplifiers, and bandpass filters from the accelerometer systems at Pump Stations 9, 10, and 11, these being the three closest instruments in the Alyeska monitoring system to the Denali fault. Here, only the results for PS10 are reported.

Table 1 gives the coordinates of site PS10 and the orientation of the accelerometers. The nominal north and east azimuths are in quotes. To establish the sensor azimuth, we used differential-GPS points along a 149-m-long laser bore-sight line pointed along the direction of a stiff plastic and aluminum jig. This jig was in turn held firmly to the side of the 6.1-cm-wide aluminum mounting block upon which the accelerometers were

Table 1. Location and orientation of the accelerometers at Pump Station 10

PS10	Value	Est. Error	Datums
Latitude	63.4244944	0.0000009[5]	ITRF00[1]
Longitude	−145.762664	0.0000020[5]	ITRF00[1]
Elevation (m)	726.1	0.4	NGVD29
"North" azimuth[2,3]	316.7	1.1	
"East" azimuth[2,3]	46.7	1.1	
"North" dip (deg)[4]	0.2	0.2	
"East" dip (deg)[4]	0.2	0.2	

[1] WGS84(G1150)~ITRF00~IGS00 (Geographic coordinate reference frames)
[2] 2GPS positioning of points along laser bore-sight line from jig held to face of accelerometer mounting block.
[3] Weighted average of azimuths from station to points along bore-sight line; in degrees clockwise from true north.
[4] Dip is relative to instrument coordinates, using machinist's bubble level and large protractor; positive dip is down.
[5] Sensor location determined with GPS has 10 cm accuracy

mounted. We noted a 4.4° counterclockwise rotation of the measured orientation from the nominal orientation (321.06°) reported in the header of the field recordings and probably based on the local "plant coordinates" and the assumption that the contractor building the 5′×5′×2′-thick pad for the instrument (1.52 m×1.52 m×0.61 m) oriented the pad precisely.

Static calibration of the three individual sensors was performed on a portable tilt table on site. No nonlinearities above the 0.3% resolution of the method were observed. Sensor gains were found to be within 0.2% of the stated values. We used a vertical step jig to test the ability of an accelerometer to measure a permanent displacement. The jig is a parallelogram of thick acrylic that partially folds and unfolds to rigid stops. The step jig held the accelerometer aligned rigidly vertical and moved it through a six-inch (15.24 cm) vertical step, either up or down. The jig and accelerometer remained in the up or down position for three minutes before and after each step motion. The duration of the step motion was about 5 s, approximating the strong-motion duration in the 2002 earthquake. Displacements were derived from a 60-s window centered on the step. The test accelerogram was first integrated to velocity and a 3rd-order polynomial (a cubic) was fitted to the start and end of the interval to establish a baseline correction used to integrate the record to displacement (see RECORD PROCESSING below). Test displacements recovered from the horizontal accelerometers were stable to within 1 cm over 60 s and recovered the step to within 2%, measured from just before to just after the step interval. The vertical sensor performed less well, producing a 4-cm baseline instability over the 60 s integration window for upward (but not downward) displacement, possibly because of minor hysteresis in the accelerometer.

Table 2. Complex filter coefficients and approximate Butterworth equivalents

		Stage 1 (0.086-Hz high-pass)[1]						
		Pole 1[3]		Pole 2[3]				
Site	Chan	Real	Imag	Real	Imag	Zero 1	Zero 2	−3 dB
PS10	V	−0.38598	0.37076	−0.38598	−0.37076	0+0i	0−0i	0.08619
	"N"	−0.38179	0.37188	−0.38179	−0.37188	0+0i	0−0i	0.08711
	"E"	−0.38209	0.36884	−0.38209	−0.36884	0+0i	0−0i	0.08617
		Stage 2 (40-Hz low-pass)[2]						
		Pole 1[3]		Pole 2[3]				
Site	Chan	Real	Imag	Real	Imag			−3 dB
PS10	V	−180.97	178.79	−180.97	−178.79	⋯	⋯	39.12
	"N"	−183.70	174.02	−183.70	−174.02	⋯	⋯	40.46
	"E"	−179.26	176.13	−179.26	−176.13	⋯	⋯	39.61

[1] Stage 1 is nominally a 2-pole Butterworth high-pass filter, with cutoff (down 3 dB) at 0.086 Hz.
[2] Stage 2 is nominally a 2-pole Butterworth low-pass filter, cutoff (down 3 dB) at 39.7 Hz.
[3] Pole values are in radians per second and associated gain values are direct out/in ratios.
[4] The Stage 2 low-pass filter does not have zeros.

The response characteristics of the electronics were verified in the USGS lab in Menlo Park. The 2-pole high-pass filter with a nominal corner of 0.1 Hz was of particular interest. In the original dissemination of the PS10 data, the high-pass filter was incorrectly specified as a 1-pole filter and the filter corner was incorrectly reported as 0.01 Hz. Ellsworth et al. (2004) assumed a 0.1-Hz corner frequency and a Butterworth response, based on the circuit diagram of the filter. The measured values (Table 2) revealed that the response was only approximately of Butterworth design (the real and imaginary parts of the poles are not equal) and that the corner was at 0.086 Hz.

The total system gain was also found to be slightly greater than the nominal values. Gain corrections of 1.012351, 1.014741, and 1.011554 were used for the processing of the "North," "East," and vertical components, respectively, reported in this paper and available on the web site. The accelerations reported here may have a residual scale error of no more than 1.5%.

RECORD PROCESSING

The Denali fault earthquake produced three separate triggers at PS10. The first was followed by 92 s of data, with the earliest earthquake energy appearing 8.4 s (1,685 samples) into the record. The second trigger was followed by 56 s of data, but unfortunately did not occur until 0.3 s after the end of the first record. This second record also contains two data spikes near its beginning, and consequently, no attempt is made here to merge these recordings. The third trigger (56 s) overlaps the second. While only the first

record is considered in this paper, we believe that it would be possible to merge the three records, albeit with some effort.

The first step in the processing of the PS10 records was to restore the low-frequency energy removed by the high-pass filters applied to the accelerograms. This deconvolution was accomplished in the frequency domain by dividing each accelerogram by the impulse response of the high-pass filter. At the four lowest frequencies the modulii of the high-pass filter's Fourier transform were: 0.00023 (D.C.), 0.01646, (0.01085 Hz), 0.06491 (0.02170 Hz), and 0.14408 (0.03255 Hz). We found that the spectral division operation was stable and that it was unnecessary to set artificially a minimum size (a "water level") for the filter impulse response spectrum. (The accelerograms were not examined for content above 40 Hz, as the power at frequencies greater than 40 Hz was more than 60 dB below the peak power in the record.)

The second step in the processing addresses the problem of the selection and placement of an acceleration baseline. Before the earthquake begins and long after it is over the sensor can be assumed to be stationary so that the expected values of both the acceleration and velocity are zero. After correction for the high-pass filter, however, neither of these conditions is met, principally because of the amplification of long-period noise (with the long-period signal) during the filter removal process. A change in the tilt of the sensor would also produce an apparent acceleration (a 1-degree tilt of a horizontal accelerometer is equivalent to an acceleration of 17 cm/sec^2). To satisfy the constraints on the velocity and acceleration, we adjust the baseline of the velocity record. A smooth cubic polynomial is best fit to the data preceding the P-wave arrival and the last 30 s of the record. These time intervals avoid the high-amplitude middle section of the record, and we can be reasonably certain that both constraints apply. The coefficients of the cubic polynomial are determined using a robust L1 (least absolute value) regression. Subtracting the polynomial from the velocity trace defines the baseline-adjusted velocity record. We further set the velocity to zero immediately preceding the P-wave arrival to obtain the corrected velocity. Integration of this record yields the corrected displacement time series, and differentiation yields the corrected acceleration time series.

In Figure 3 we compare the corrected records with the original recordings for an unrotated component of motion (N136.7°E), roughly parallel to the Denali fault. The changes in both the velocity and displacement records are dramatic due to the restoration of the long-period components of the signal that are suppressed in the original filtered data. Subtracting the original accelerograms from the processed data reveal low-frequency differences with peak values of up to 102 cm/sec^2 and 39 cm/sec^2 in the horizontal and vertical components, respectively. At frequencies greater than 0.25 Hz, the coherency between the original and processed records exceeds 0.99 and the spectral amplitudes agree within 1%.

The instrument-corrected acceleration, velocity, and displacement time series are available at: ftp://clover.wr.usgs.gov/pub/ehz/PS10.

GROUND MOTION AT PUMP STATION 10

Figure 4 presents the instrument-corrected acceleration after rotation into fault-oriented coordinates, using a fault strike of N111.62°E as the reference fault-parallel

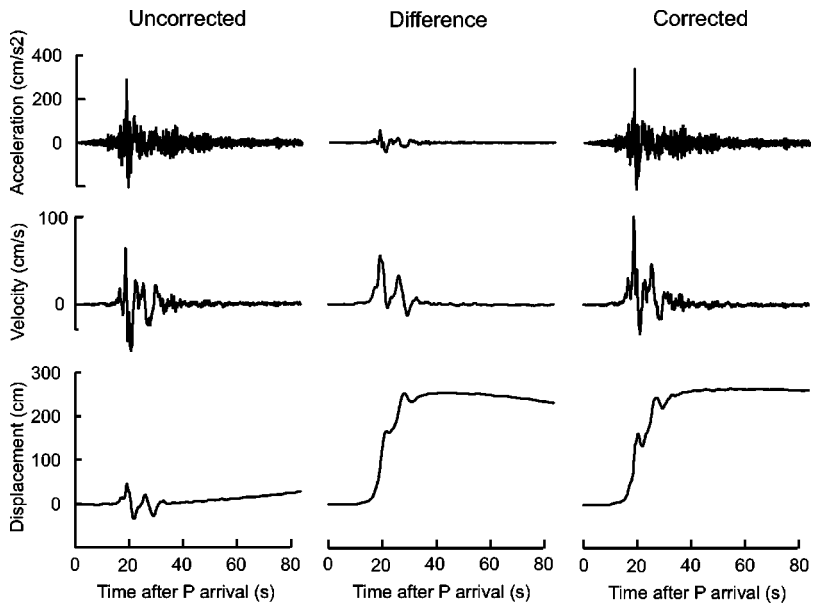

Figure 3. Example of instrument correction for unrotated component of motion (N136.7 °E) Pump Station 10 acceleration (top row), velocity (middle row) and displacement (bottom row). Left column: original field recordings. Right column: instrument-corrected accelerations. Middle column is the difference between the right and left columns and represents the component of the ground motion recovered from the field recordings by deconvolution of the 0.086-Hz high-pass filter.

(FP) direction. This direction approximates the regional strike of the Denali fault, and was selected to match the permanent displacement of survey marks near PS10 determined during a GPS survey by Alyeska shortly after the earthquake. The local strike direction is somewhat more clock-wise at N121 °E. The reference fault-normal (FN) direction is N21.62 °E and the vertical component is positive upward. Our processed record starts at the P-wave arrival, which occurs at 22:12:56.36 UCT, according to the GPS clock in the instrument.

Peak accelerations on the three components are 286 cm/s^2 (FN), 313 cm/s^2 (FP), and 242 cm/s^2 (V). The peak vector horizontal acceleration is 360 cm/s^2. An impulsive, double-sided pulse (swinging to both directions) near the beginning of the high-acceleration portion of the record dominates the motion on all three components. This pulse lasts only 1.5 s. The high-amplitude portion of the record (amplitudes greater than 0.1 g) lasts significantly longer on the FN component than on the FP component.

The acceleration pulse integrates on the FP component to a single-sided pulse with a peak velocity of 157 cm/s that dominates the FP velocity record (Figure 5). The peak velocities on the FN component (108 cm/s) and V component (42 cm/s) also occur during this pulse. Strong oscillatory motions continue on the FN component for an additional 10 s, but are substantially weaker on the FP component.

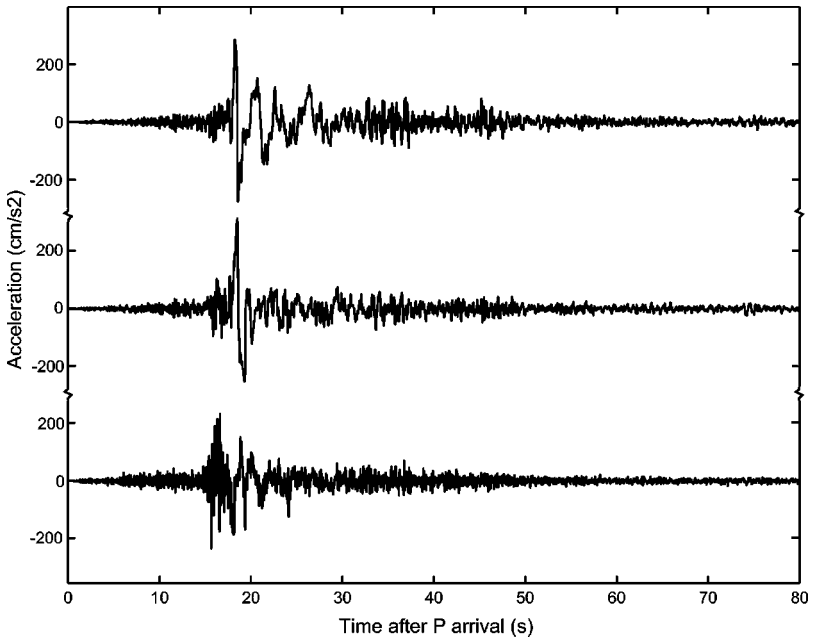

Figure 4. Accelerations after instrument correction in fault-oriented coordinates. Fault-normal (FN), top; fault-parallel (FP), middle; up (V), bottom.

The FP displacement time series is a smoothed-step-like pulse that grows almost monotonically to its permanent displacement of 2.98 m (Figure 6). This step-like displacement pulse has been called the "fling step" (Bolt and Abrahamson 2003). About half of its total displacement occurs during the high-velocity FP pulse. The FN displacement is a single-sided pulse of 8-s duration with a peak displacement of 1.08 m corresponding to the "directivity pulse" of Bolt and Abrahamson (2003). The permanent horizontal displacement of PS10 recovered from the instrument-corrected accelerograms agrees well with the displacement of 3 m determined by the GPS survey made by Alyeska (Figure 7).

Particle-motion diagrams of the velocity and displacement reveal several important features of the ground motion (Figure 7). These diagrams portray the movement of PS10 in the horizontal plane. The high-velocity portion of the record begins 18 s after the P-wave arrival with a large clockwise loop comprised initially of almost equal parts of FN and FP motion that attains a peak velocity (combined FN and FP) of 181 cm/s. Following this first large velocity pulse, the strongest motion occurs principally on the FN component, with major velocity peaks at 21, 25 and 28 s.

Both the timing and direction of motion during the first large-velocity pulse and displacement surge (between 18 s and 19.5 s) strongly suggest that the pulse originates as the rupture is passing PS10, and that the short duration of the pulse is caused by directivity. (A station in line with an approaching rupture sees a Doppler-effect compression of data.) The pulse arrives 33.5 s after the origin time of the earthquake (on the Susitna

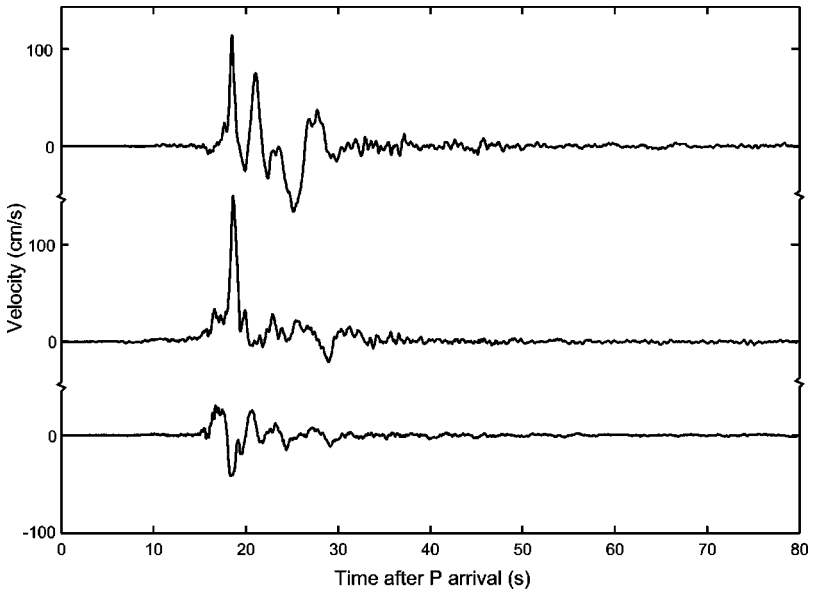

Figure 5. Velocity after instrument correction in fault-oriented coordinates. Fault-normal (FN), top; fault-parallel (FP), middle; up (V), bottom.

Glacier fault). When the delay for S-wave propagation to PS10 from the nearest point on the fault plane is taken into account, the rupture can be inferred to pass PS10 at about 32.5 s after the origin time, implying an average propagation velocity of 2.8 km/s or roughly 75% to 80% of the crustal shear-wave velocity. This estimate of average rupture velocity is a lower bound because the 32.5 s includes possible delays between the failure of the Susitna Glacier fault and the initiation of strike-slip faulting on the Denali fault. Evidence of spatial variation of rupture velocity along the fault is discussed below.

A rough estimate of soil strain, based on peak ground velocity, indicates that there was probably nonlinear soil response at PS10. Stokoe et al. (2004) show that well-graded gravels are more prone to nonlinear response than are well-graded sands and low-plasticity and high-plasticity clays. Significant modulus reduction occurs in such gravels at shear strains of 0.01%. At distances represented by PS10, S-waves propagate nearly vertically, so vertical strains (that is, d/dz) would be expected to dominate at sufficient depth from the free surface. At frequencies above 2 Hz, the quarter-wave skin depth of the free-surface effect is less than the thickness of the gravels (assumed to be 40 m, based on the shear-velocity profile of Kayen et al. 2004 (this issue), and the borehole log), so high vertical strains would be expected in the deeper part of the gravels for frequencies above 2 Hz. A rough estimate of the strain is the peak horizontal velocity (about 1 m/s) divided by the S-wave speed, 316 m/s, or about 0.3%, which is well into the nonlinear range established by Stokoe et al. (2004).

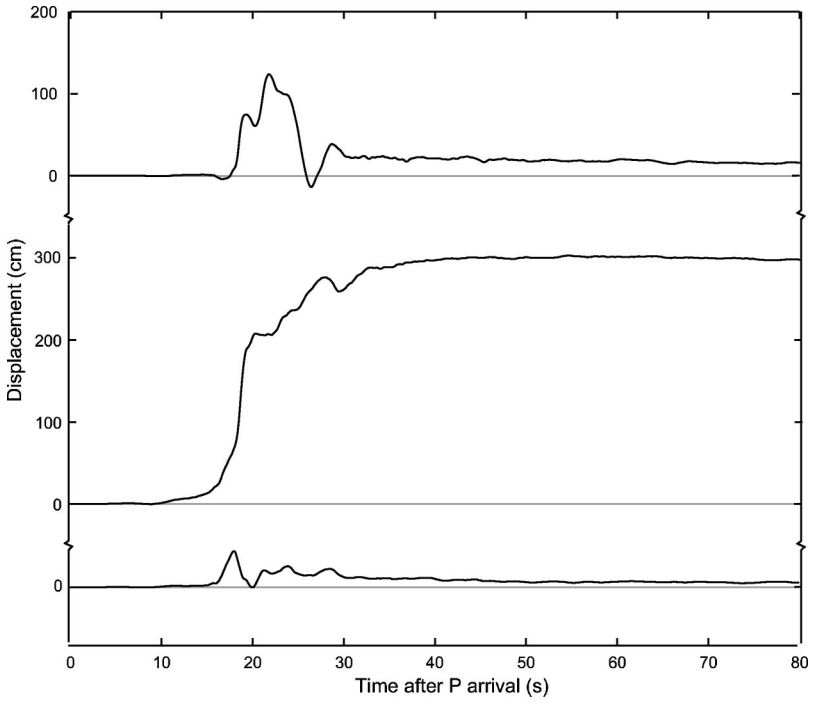

Figure 6. Displacement after instrument correction in fault-oriented coordinates. Fault-normal (FN), top; fault-parallel (FP), middle; up (V), bottom.

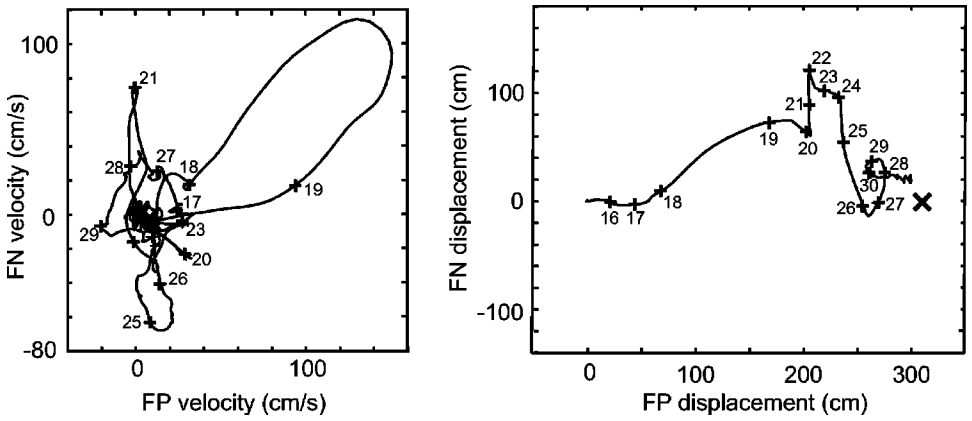

Figure 7. Particle motion diagram for velocity (left) and displacement (right) in the fault-normal (N21.62 °E) and fault-parallel (N111.62 °E) directions. Crosses labeled at 1-s intervals after start of records. "×" indicates permanent displacement of Pump Station 10 determined by GPS survey.

Table 3. Crustal structure

Depth (km)	P-wave speed (km/s)	S-wave speed (km/s)
0	5.0[1]	2.6[1]
3	6.0[1]	3.46[1]
10	6.45[1]	3.72[1]
40.5	6.45	3.72
40.5	6.8	3.93
49	6.8	3.93
49	8.2	4.73

[1] Linear interpolation used between depths

IMPLICATIONS FOR THE FAULTING PROCESS

Forward modeling of the PS10 ground displacement and velocity time series has led to the derivation of a plausible model for the rupture involving super-shear rupture velocity. Because of its proximity to the fault, PS10 is most strongly affected by the portion of the fault within 15 km and at depths between 0 and 5 km, as demonstrated below. Consequently, we can only comment on the rupture behavior on this nearby portion of the Denali fault. We used the COMPSYN method of Spudich and Xu (2003a), which calculates the complete synthetic ground motion in a vertically varying, non-attenuating earth structure. The Denali fault was approximated by a vertical plane extending approximately 65 km NW and 55 km SE of PS10 and extending to 12 km depth, passing 2.87 km from PS10. We assumed that the observed horizontally varying surface slip (both strike-slip and dip-slip components) reported by Eberhart-Phillips et al. (2003) extended from the surface to the assumed 12-km depth (motion at PS10 was insensitive to the extent of faulting depth). We used a vertically varying velocity structure (Table 3) based on Brocher et al. (1991 and submitted). This model omitted the low surface velocities observed by Kayen et al. (2004) to reduce computation time and to prevent the buildup of large surface waves, which would not be expected in a laterally varying, attenuating structure. The slip-velocity time function was assumed to be a decaying exponential with 1-s time constant everywhere.

The ground motion at PS10 is best matched in this model by a rupture traveling at a speed of 1.5 times the shear wave speed in the crust (i.e. about 5.3 km/s at 5 km depth) as it passes PS10. The polarizations of the PS10 velocities and displacements were a strong constraint suggesting high rupture velocity near PS10. The observed FP velocity (Figure 5) shows a strong, sharp one-sided pulse that arrives simultaneously with a sharp one-sided pulse on the FN velocity. Also, the FP ramp in displacement (Figure 6) arrives earlier than the FN displacement pulse (Figure 7). The near-simultaneous arrival of the FN and FP velocity pulses, and the delay of the FN displacements after the FP displace-

ments are characteristics of the data that we found difficult to produce using sub-shear rupture velocities. This is in accord with the synthetic modeling of Aagaard and Heaton (submitted).

Our rupture model has a ratio V_r/V_s of rupture velocity V_r to shear velocity V_s of 0.65 on the portion of the fault farther west than 18 km from PS10, 1.5 from 18 km west to 20 km east of PS10, and 0.85 farther than 20 km east of PS10. The primary control on the high rupture velocity segment near PS10 is polarization, as discussed above. The low rupture velocity ($V_r/V_s=0.65$) is poorly resolved; given the high rupture velocity close to PS10, the rupture must be delayed by a slower rupture before reaching the high rupture velocity segment. The 0.65 ratio is a lower bound for this segment because it assumes a straight fault, rather than a longer arc-like fault connecting the hypocenter and PS10. Ground motion amplitudes at PS10 are insensitive to rupture velocity on this segment, and the actual rupture velocity on this segment could be higher if the rupture is delayed in jumping from the Susitna Glacier fault to the Denali fault. Our rupture velocity of $0.85V_s$ east of PS10 is a nominal value; we have no resolution of rupture velocity in this region, and we did not test other possible velocities. Figure 8 shows the synthetic velocities from our preferred rupture model. Peak horizontal ground velocity is predicted very well from this simple source model, considering that there are only four free parameters in our rupture model, namely the rupture velocities on the fault segments west of, and adjacent to, PS10, the location of the rupture velocity jump, and the rise time. Our model overpredicts peak vertical ground velocity by a factor of 3. The synthetic FP velocity pulse is one-sided, a characteristic difficult to produce with a rupture traveling at a sub-shear velocity. The synthetic horizontal pulses in Figure 8 arrive about 1 s earlier than the data, but this is a negligible problem that could easily be remedied by allowing a 1-s delay in the jumping of the rupture from the Susitna Glacier fault to the Denali fault.

The large horizontal velocity pulse in our rupture model is caused by a local minimum of the arrival time function, a consequence of the super-shear rupture velocity. Figure 9 shows contours (isochrones) of the arrival time function superimposed on a plot of the amplitude of the fault-parallel S-wave radiation emitted from each point on the fault and received at PS10. Contours labeled t show the points on the fault that radiate S waves which arrive at PS10 at time t. (Actually, owing to the finite rise time of slip on each point of the fault, the contours show the leading edge of a narrow advancing band on the fault contributing S waves.) The plotted color function is $|\Psi_x^s|$ (Spudich and Xu 2003b, Equation 27.2), which is the product of the slip, geometric spreading factor, radiation pattern, directivity factor (isochrone velocity), and impedance factors which contribute to the S-wave amplitude at PS10. This function is large only near PS10, demonstrating that PS10 is only affected by the nearby portion of the Denali fault. Figure 9 shows that at about time 32.6 s, S waves are arriving from a region about 30 km east of PS10 (along-strike coordinate: -30 km) and also from about 5 km east of PS10, which is the location of a local minimum in the arrival time function. Super-shear rupture velocity causes this local minimum, which physically signifies the formation of a Mach cone, which causes the high-velocity pulse as it sweeps by PS10. Numerical simulations by Aagaard and Heaton (submitted) show the development of this Mach cone in super-

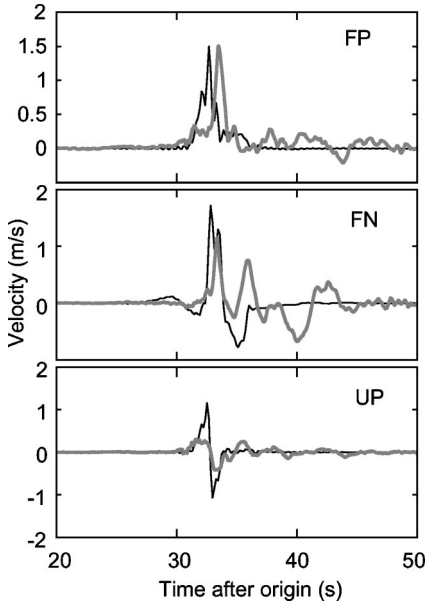

Figure 8. Comparison of fault-parallel (top), fault-normal (middle) and vertical (bottom), observed (gray) and synthetic (black) ground velocity. Synthetic motions are calculated for a model with a low initial rupture velocity, a fast rupture velocity (1.5 times the shear wave velocity) as the rupture passes PS10, and a subsequent slower rupture velocity. The FP pulse is one-sided, and the main peaks on the horizontal components occur approximately simultaneously.

shear rupture. For comparison, Figure 10 shows a similar plot for a uniform sub-shear rupture velocity (73% of the local shear velocity), for which no local minimum of the arrival time function (nor the associated Mach cone) occur.

Our analysis indicates that super-shear rupture velocity near PS10 is a plausible interpretation of the data. Other explanations are undoubtedly possible, as the record at a single observation point cannot uniquely define the detail, in both space and time, of the rupture. In fact, we know that the rupture process must have been more complex than depicted by our simple rupture model, as this model cannot explain the prominent velocity pulses on the FN component that follow the passage of the rupture front. By permitting greater variability both in the fault displacement, particularly as a function of depth, and in the acceleration and deceleration of the rupture front, alternative models could be constructed that match the observations better.

RESPONSE SPECTRA AND ATTENUATION RELATIONS

Short-period ground motions observed at PS10 were lower than motions predicted by two often-used empirical ground-motion prediction relations ("attenuation relations") derived from smaller earthquake data, implying that these prediction relations might yield overpredictions when extrapolated to magnitudes higher than their recom-

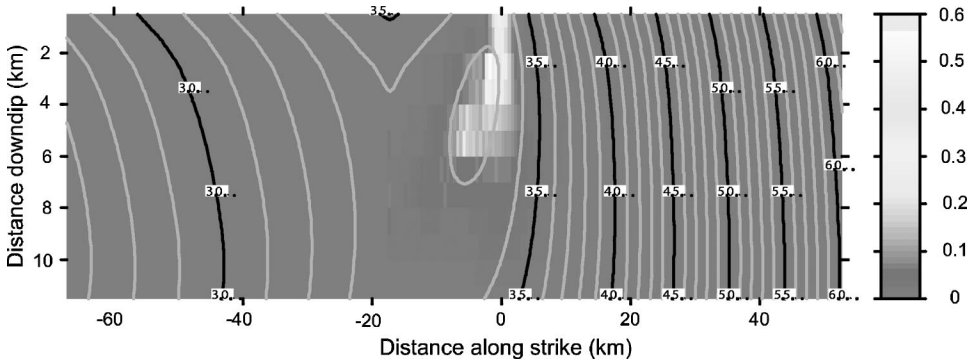

Figure 9. Plot, for the case of supershear rupture velocity, of two quantities on the portion of the Denali fault surface extending from the surface to 12 km depth and from 68 km east to 53 km west of PS10, located at 0 km along strike. Contours are isochrones of the arrival time function. A contour labeled with *t* shows the points on the fault radiating S-waves which arrive at PS10 at time *t*. Fill colors show contribution of S-wave radiation from each point to the fault-parallel displacement at PS10. Points within 5-10 km of PS10 at depths less than 6 km dominate the motion at PS10. Supershear rupture velocity causes a local minimum of the arrival time function at about 32.6 s, which causes the large fault-parallel velocity pulse at that time. See text for further details.

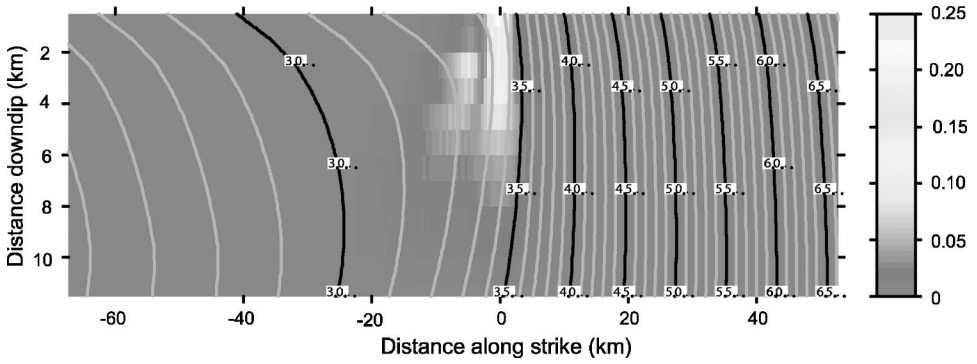

Figure 10. Plot, for the case of subshear rupture velocity, of two quantities on the portion of the Denali fault surface extending from the surface to 12 km depth and from 68 km east to 53 km west of PS10, located at 0 km along strike. Contours are isochrones of the arrival time function. A contour labeled with *t* shows the points on the fault radiating S-waves which arrive at PS10 at time *t*. Fill colors show contribution of S-wave radiation from each point to the fault-parallel displacement at PS10. Points within 5-7 km of PS10 at depths less than 5 km dominate the motions at PS10. The fill color scale differs from that in Figure 9. See text for further details.

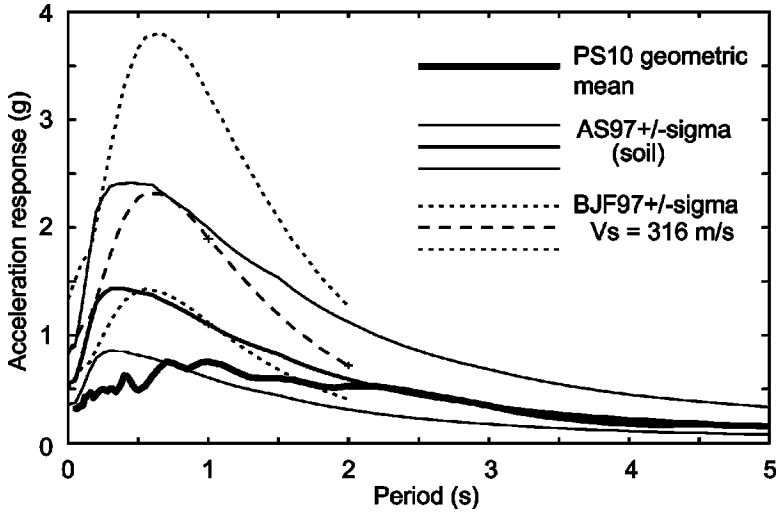

Figure 11. Comparison of the geometric mean of the horizontal elastic spectral acceleration (5% damping) for PS10 (thickest line) and the spectral acceleration (± one standard deviation) predicted by the empirical relation of Abrahamson and Silva (1997) (thin lines) and the pseudo-spectral acceleration of Boore et al. (1997) (dashes).

mended range. Because there is only one near-fault accelerogram from this earthquake, we cannot say whether the Denali fault earthquake had relatively low accelerations everywhere. Figure 11 shows a comparison of observed geometric-mean horizontal elastic spectral acceleration (5% damping) with both the predicted motion for an M7.9 strike-slip event on a vertical fault observed at a 2.87-km distance using the empirical relation for spectral acceleration of Abrahamson and Silva (1997) for this soil site condition and the pseudo-spectral acceleration derived from the relation of Boore et al. (1997) for a 30-m shear-wave velocity of 316 m/s. The geometric mean spectrum at a period T is the square root of the product of the fault-normal and fault-parallel spectra at the period T. For periods less than 1 s, the predicted spectral acceleration is 1-2 standard deviations above the observed motion. Observed accelerations in the 1999 M7.4 Izmit, Turkey, earthquake and the 1999 M7.6 Chi-Chi, Taiwan, earthquake have also been lower than predicted based on attenuation relations derived from smaller events at larger distances, implying that some factors might be causing the scaling of ground motion with magnitude to change for large events (Somerville 2000, Anderson et al. 2000, Boore 2001, Anderson 2003). Relatively low accelerations have been correlated with earthquakes having surface fault rupture by Somerville (2000), a pattern which the 2002 Denali fault earthquake fits, but other possible causes for low accelerations at PS10 might be the rupture velocity exceeding the shear-wave velocity, as discussed later, or nonlinear response in gravels at the site, as discussed above. Displacement response spectra are relevant to the design of flexible structures. Figure 12 shows 5%-damped displacement response spectra for the fault-parallel, fault-normal, and geometric mean horizontal motion at PS10.

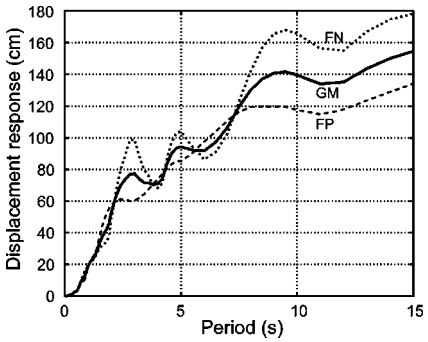

Figure 12. Elastic displacement response (5% damping) for the fault-normal component (dotted), fault-parallel component (dashed), and geometric mean horizontal (solid line) motion at PS10.

The PS10 response spectral shapes can be compared with those in the building codes. However, we compare only with the *UBC94* because it is easy to compare the observed response spectral shapes to the *UBC94* for a given site class. The *IBC2003* cannot be easily compared because the code response spectrum cannot be directly normalized to zero-period acceleration. Figure 13 shows the 5%-damped and normalized elastic response spectra computed from the FN and FP accelerations. Also superimposed on the spectra is the *UBC94* normalized response spectrum for site class 3. The normalized response spectra of the recorded motion exceeds the normalized *UBC94* code spectrum by a factor as much as 2 between 2 s and 3.5 s for FN motions and by a factor as much as 1.5 between 1.5 s and 3 s for the FP motions. These high spectral amplitudes correspond to the long-period excursions evident in Figure 6. They would affect the strength and ductility demands on structures with fundamental periods within the stated period ranges.

DISCUSSION AND CONCLUSIONS

Although we have only one near-fault recording from this earthquake, at PS10, the short-period ground motion there is lower than predicted by empirical ground-motion prediction relations developed from smaller magnitude events, a discrepancy also observed for the 1999 M7.4 Kocaeli (Izmit), Turkey, earthquake (Anderson et al. 2000) and the M7.6 Chi-Chi, Taiwan, earthquake (Boore 2001). This discrepancy might mean that large earthquakes rupture differently from smaller ($M<7.4$) earthquakes, and this discrepancy could have implications for current probabilistic seismic hazard assessments.

The high-frequency motion at PS10 might have been reduced by nonlinear soil response. Additionally, we speculate that it might also have been reduced by a super-shear rupture velocity, which might occur more commonly in large crustal earthquakes than in moderate-sized events. Possible super-shear rupture velocity has been suggested in the 1999 M7.4 Kocaeli earthquake (Bouchon et al. 2000) and in the 2001 M8.1 Kunlunshan earthquake (Bouchon and Vallée 2003), although the evidence is not conclusive owing to the relatively poor data sets from these events. Super-shear rupture velocity was not

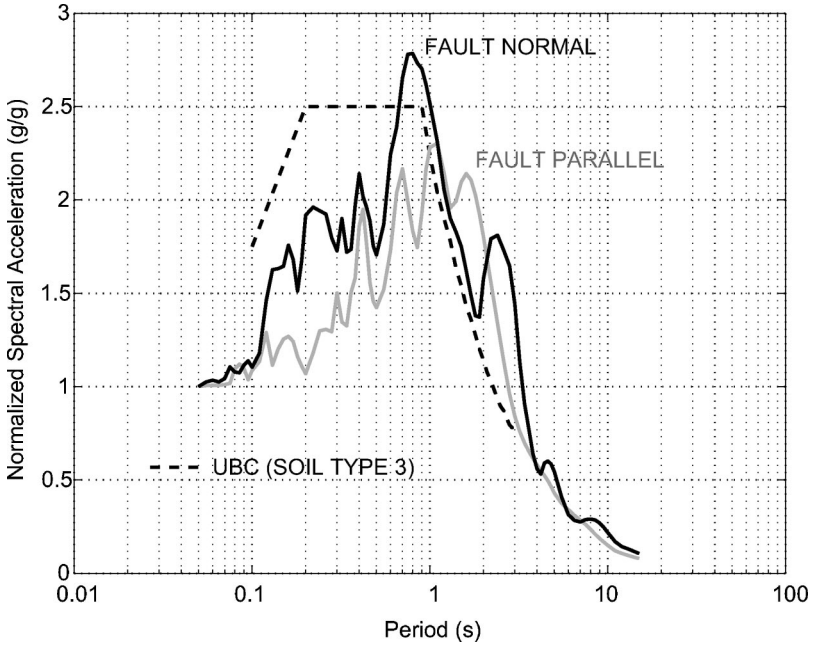

Figure 13. Normalized elastic response spectra (5% damping) for the FN (black) and FP (gray) components of acceleration at PS10. Each response spectrum is normalized to 1 g by dividing the spectral ordinates by the zero-period acceleration (ZPA). Also shown is the *1994 Uniform Building Code* (*UBC94*) normalized response spectrum for site class 3 (dashed).

documented in the 1999 M7.6 Chi-Chi earthquake. That is to say, three out of four large crustal earthquakes observed from 1999 on have had some evidence of super-shear rupture velocities. A consequence of super-shear rupture velocity is that the order of the singularity in slip velocity at the crack tip diminishes, resulting in less high-frequency energy radiation (Burridge 1973). However, a compensating effect is that super-shear rupture velocity can cause singularities in isochrone velocity. These singularities, which occur at local minima of the arrival time function, such as in Figure 9, would enhance high-frequency motion in specific directions (Spudich and Frazer 1984). Further study will be needed to confirm whether super-shear rupture velocity causes diminished ground acceleration in some large earthquakes.

Despite the relatively low-amplitude short-period motion, the long-period ground response at PS10 was substantial. Thus the PS10 motion confirms what has been previously observed in other, rare near-fault recordings by Heaton et al. (1995), namely, high-velocity, 1-s to 3-s duration pulses result in large displacements of structures with similar long periods, even when the accelerations are modest. Large ground-motion pulses can cause large displacements, which should be considered during the structural design and analysis process in order to balance strength and ductility considerations properly.

ACKNOWLEDGMENTS

We thank Russell Sell, who participated in the field calibration of the PS10 instrumentation, Janise Rodgers, and Arthur Frankel, who reviewed the manuscript, and Artak Martirosyan and Sharon Wood for additional helpful input.

REFERENCES

Aagaard, B. T., and Heaton, T. H., Near-source ground motions from simulations of sustained intersonic and supersonic fault ruptures, submitted to *Bull. Seismol. Soc. Am.*

Abrahamson, N. A., and Silva, W. J., 1997. Empirical response spectral attenuation relations for shallow crustal earthquakes, *Seismol. Res. Lett.* **68**, 94–127.

Anderson, J. G., 2003. Strong-motion seismology, in *International Handbook of Earthquake and Engineering Seismology*, W. H. K. Lee, H. Kanamori, P. C. Jennings, and C. Kisslinger (editors), Academic Press, New York, Part B, ch. 57, pp. 937–966.

Anderson, J. G., Brune, J. N., Anooshehpoor, R., and Ni, S. D., 2000. New ground-motion data and concepts in seismic hazard analysis, *Curr. Sci.* **79**, 1278–1290.

Bolt, B. A., and Abrahamson, N. A., 2003. Estimation of strong seismic ground motions, in *International Handbook of Earthquake and Engineering Seismology*, W. H. K. Lee, H. Kanamori, P. C. Jennings, and C. Kisslinger (editors), Academic Press, New York, Part B, ch. 59, pp. 983–1001.

Boore, D. M., 2001. Comparisons of ground motions from the 1999 Chi-Chi earthquake with empirical predictions largely based on data from California, *Bull. Seismol. Soc. Am.* **91**, 1212–1217.

Boore, D. M., Joyner, W. B., and Fumal, T. E., 1997. Equations for estimating horizontal response spectra and peak acceleration from western North American earthquakes: A summary of recent work, *Seismol. Res. Lett.* **68**, 128–153.

Bouchon, M., Toksöz, N., Karabulut, H., Bouin, M. P., Dietrich, M., Aktar, M., and Edie, M., 2000. Seismic imaging of the 1999 Izmit (Turkey) rupture inferred from the near-fault recordings, *Geophys. Res. Lett.* **27**, 3013–3016.

Bouchon, M., and Vallée, M., 2003. Observation of long supershear rupture during the magnitude 8.1 Kunlunshan earthquake, *Science* **301**, 824–826.

Brocher, T. M., Fuis, G. S., Lutter, W. J., and Christensen, N. I., Seismic velocity models for the Denali fault zone along the Richardson Highway, Alaska, submitted to *Bull. Seismol. Soc. Am.*

Brocher, T. M., Nokleberg, W. J., Christensen, N. I., Lutter, W. J., Geist, E. L., and Fisher, M. A., 1991. Seismic reflection/refraction mapping of faulting and regional dips in the eastern Alaska Range, *J. Geophys. Res.* **96**, 10233–10249.

Burridge, R., 1973. Admissible speeds for plane-strain self-similar shear cracks with friction but lacking cohesion, *Geophys. J. Roy. Astron. Soc.* **35**, 439–455.

Campbell, K. W., and Bozorgnia, Y., 2003. Updated near-source ground-motion (attenuation) relations for the horizontal and vertical components of peak ground acceleration and acceleration response spectra, *Bull. Seismol. Soc. Am.* **93**, 314–331.

Eberhart-Phillips, D., and 28 coauthors, 2003. The 2002 Denali fault earthquake, Alaska: A large-magnitude, slip-partitioned event, *Science* **300**, 1113–1118.

Electric Power Research Institute, 1993. *Guidelines for Site-Specific Ground Motions*, Appendix 2A, EPRI TR-102293, 2, Palo Alto, CA.

Ellsworth, W. L., Celebi, M., Evans, J. R., Jensen, E. G., Nyman, D. J., and Spudich, P., 2004. Processing and modeling of the Pump Station 10 record from the November 3, 2003, Denali fault, Alaska, earthquake, *Proceedings, 11th International Conference on Soil Dynamics and Earthquake Engineering*, vol. 1, Berkeley, California, pp. 471–477.

Hall, W. J., Nyman, D. J., Johnson, E. R., and Norton, J. D., 2003. Performance of the trans-Alaska pipeline in the November 3, 2003 Denali fault earthquake, *Proceedings of the Sixth U.S. Conference and Workshop on Lifeline Earthquake Engineering*, ASCE Technical Council on Lifeline Engineering, Long Beach, CA.

Heaton, T. H., Hall, J. F., Wald, D. J., and Halling, M. W., 1995. Response of high-rise and base-isolated buildings to a hypothetical Mw 7.0 blind thrust earthquake, *Science* **267**, 206–211.

International Code Council, 2002. *2003 International Building Code*, Falls Church, VA.

International Conference of Building Officials, 1994. *Uniform Building Code*, Whittier, CA.

Kayen, R., Thompson, E., Minasian, D., Collins, B., Moss, E. R. S., Sitar, N., and Carver, G., 2004. Geotechnical reconnaissance of the 2002 Denali fault, Alaska, earthquake, *Earthquake Spectra* **20** (3), 639–667 (this issue).

Lee, W. H. K., Shin, T. C., Kuo, K. W., Chen, K. C., and Wu, C. F., 2001. CWB free-field strong-motion data from the 21 September Chi-Chi, Taiwan, earthquake, *Bull. Seismol. Soc. Am.* **91**, 1370–1376.

National Soil Services, 1971. Log of boring no. 10-6 & P-6, Pump Station No. 10, unpublished, dated April 18, 1971. Available: http://nsmp.wr.usgs.gov/borehole/taps_logs.html

Somerville, P. G., 2000. Magnitude scaling of near fault ground motions, *American Geophysical Union*, *Fall Meeting Supplement*, vol. 81, p. F822, Available at http://www.agu.org.

Somerville, P. G., 2003. Magnitude scaling of the near fault rupture directivity pulse, *Physics of the Earth and Planetary Interiors* **137**, 201–212.

Spudich, P., and Frazer, L. N., 1984. Use of ray theory to calculate high-frequency radiation from earthquake sources having spatially variable rupture velocity and stress drop, *Bull. Seismol. Soc. Am.* **74**, 2061–2082.

Spudich, P., and Xu, L., 2003a. Software for calculating earthquake ground motions from finite faults in vertically varying media, in *International Handbook of Earthquake and Engineering Seismology*, W. H. K. Lee, H. Kanamori, P. C. Jennings, and C. Kisslinger (editors), Academic Press, New York, Part B, ch. 85-14, pp. 1633–1634.

Spudich, P., and Xu, L., 2003b. Documentation of software package ISOSYN v3.11: isochrone integration programs for earthquake ground motion calculation, in CD#3 accompanying *International Handbook of Earthquake and Engineering Seismology, Part B*, W. H. K. Lee, H. Kanamori, P. C. Jennings, and C. Kisslinger (editors), Academic Press, New York, Part B.

Stokoe, K. H., Darendeli, M. B., Menq, F.-Y., and Choi, W. K., 2004. Comparison of the linear and nonlinear dynamic properties of gravels, sands, silts, and clays, *Proceedings, 11th International Conference on Soil Dynamics and Earthquake Engineering*, vol. 1, Berkeley, California, pp. 1–4.

(Received 25 November 2003; accepted 13 January 2004)